Revista Mexicana de Astronomía y Astrofísica, **40**, 15–23 (2004)

HERBIG-HARO JETS EMERGING FROM A NEUTRAL CLOUD INTO A H II REGION

A. C. Raga,[1] and B. Reipurth[2]

Received 2003 June 3; accepted 2003 October 20

RESUMEN

Presentamos simulaciones numéricas de un flujo Herbig-Haro que sale de una nube densa hacia una región H II. Este tipo de "salidas" de nubes densas han sido observadas recientemente en varias regiones de formación estelar, y aquí exploramos las propiedades de estos flujos variando algunos de los parámetros libres del modelo. Presentamos series temporales de la temperatura, densidad, fracción de ionización y de la emisión en Hα. Encontramos que la emisión en Hα de los flujos está mayormente controlada por el flujo incidente de fotones ionizantes, en lugar de por las propiedades intrínsecas del flujo.

ABSTRACT

We present numerical simulations of a Herbig-Haro flow that bursts out of a dense cloud core into a surrounding HII region. Such blow-outs from cloud cores have recently been imaged in various star-forming regions, and we here explore the properties of such outflows by varying selected input parameters to the models. We present time-series of temperature, density, ionization fraction, and Hα emission. We find that the Hα emission of the outflows is mostly controlled by the impinging ionizing photon field rather than by the intrinsic properties of the outflows.

Key Words: **ISM: HERBIG-HARO OBJECTS — ISM: JETS AND OUTFLOWS — ISM: KINEMATICS AND DYNAMICS**

1. INTRODUCTION

Herbig-Haro (HH) objects are the optical manifestations of powerful mass loss that occurs in stars at all stages of early stellar evolution, from deeply embedded protostellar objects to visible young stars. In addition to being astrophysical laboratories for the analysis of shock structures, of the hydrodynamics in collimated flows, and of their interaction with the surrounding environment, HH flows provide indirect but important insights into the nature of the accretion and mass loss processes which govern the formation of stars. Indeed, when HH flows attain parsec-scale dimensions it becomes possible to partially reconstruct the mass ejection history of the newly born driving sources (and therefore their mass accretion history) for a significant fraction of the duration of the embedded phase. For a recent review of HH flows see Reipurth & Bally (2001).

Because flows from newborn stars extend in many cases over several parsecs, they frequently break out of the molecular cloud in which they originate. It has recently been realized that when a cloud core is sculpted by the UV radiation from nearby OB stars and takes a characteristic cometary shape with smooth edges, then the breakout of a flow becomes particularly easy to identify and to study. A case in point is the blow-out of two flows from the cloud core containing the S140 cluster (Bally et al. 2002), and other cases are found in the NGC 2264 star forming region (Reipurth et al. 2004). A particularly fine case has been found in the IC1396N cloud core, where the HH 777 flow is seen to break out from the dense cloud core into the surrounding H II region. Reipurth et al. (2003) discussed the properties and origin of the HH 777 flow, and presented gasdynamic calculations that matched as closely as possible the observed properties of this blow-out. In the present paper we extend the analysis of the HH 777 flow to more generalized conditions, and in a series of model calculations we explore the effect of varying input parameters on the resulting outflow. We also present a detailed discussion of the models and of the results obtained from the numerical simulations.

[1]Instituto de Ciencias Nucleares, Universidad Nacional Autónoma de México, México City, D. F., México.
[2]Institute of Astronomy, University of Hawaii, USA.

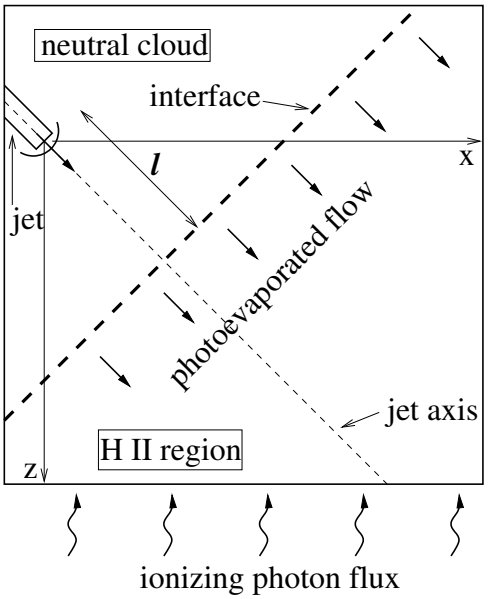

Fig. 1. Schematic diagram showing the configuration for the simulations of jets emerging from a neutral cloud into a photoionized region.

2. THE NUMERICAL SIMULATIONS

We have computed four jet models with the configuration shown in Figure 1. The $(2, 1, 2) \times 10^{18}$ cm domain (along the x, y and z axes, respectively) is divided into two regions by a planar surface parallel to the y-axis and cutting the xz-plane at an angle of $\pi/4$ to the x and z axes. On one side of this surface, we have a homogeneous, neutral cloud (of density $n_c = 1000$ cm^{-3} and temperature $T_c = 100$ K), and on the other side an H II region (of density $n_{ion} = 1$ or 10 cm^{-3} and temperature $T_{ion} = 10^4$ K, see Table 1). We should note that none of these initial configurations have pressure balance across the ionized/neutral gas boundary. However, this is not an important problem as the boundary region rapidly becomes highly overpressured (and therefore sends shocks into both the neutral and ionized regions) as a result of the impinging photoionizing flux discussed below.

A flux of ionizing photons $F_0 = S_*/4\pi D^2 = 1.60 \times 10^{10}$ cm^{-2} s^{-1} (from a far-away star of temperature $T_{eff} = 50,000$ K and ionizing photon rate $S_* = 5 \times 10^{49}$ s^{-1} at a distance $D = 10$ pc from the edge of the computational domain) enters the domain, parallel to the z-axis (i.e., the geometrical divergence of the radiation field is neglected). This ionizing photon flux hits the (plane) surface of the neutral cloud, which then starts ejecting a photoevaporated wind into the H II region (see Fig. 1).

The jet inflow condition is imposed in a cylinder of radius $r_j = 2.5 \times 10^{16}$ cm and of length 3.5×10^{17} cm. This radius is a factor of ~ 10 times larger than the ones measured for the region close to the source of typical HH jets. However, given the limited spatial resolution of our simulations (see below), this expanded initial jet radius is necessary for achieving a (barely) appropriate resolution of the initial jet cross section. The axis of the cylinder (which coincides with the outflow axis) is perpendicular to the neutral cloud/H II region boundary. The tip of the cylinder (i.e., the injection point) is at a distance $l = 9 \times 10^{17}$ cm from the initial cloud/H II region boundary (see Fig. 1).

A reflection condition is imposed on the top and left boundaries of the domain shown in Fig. 1, and a free outflow condition is applied on all other grid boundaries. The reflection conditions are, of course, not very realistic, particularly because they are applied in two planes which are oblique with respect to the outflow axis. We apply such reflection conditions anyway, because the alternative of applying a transmission condition in a subsonic flow region is even less realistic. However, because the nature of the boundaries close to the injection cross section is not very important for the case of radiative jets (which do not inflate a large, hot cocoon), this is not a fundamental issue for our simulations. An indication of the lack of importance of these boundary conditions is the fact that even though the reflection conditions have an asymmetric topology with respect to the injection cross section (see Fig. 1), the structure of the jet flow is completely symmetric (that is, before the jet exits the dense cloud, see Figure 4).

The jet is injected with a top hat cross section with a time-independent density $n_j = 1000$ cm^{-3} and temperature $T_j = 1000$ K. The ejection velocity v_j varies sinusoidally with time:

$$v_j(t) = v_0 + \Delta v \, \sin\left(\frac{2\pi t}{\tau_v}\right) , \qquad (1)$$

and we have carried out four different simulations with the combinations of τ_v, v_0 and Δv listed in Table 1.

Models M1-M3 have been computed in order to explore the differences between a jet with time-independent ejection (model M1), and variable ejection velocity jets with different periods (models M2 and M3). These three models have an on-axis post-leading bow shock cooling distance of ~ 0.2 times the initial jet diameter. Model M4 has a larger average velocity (v_0) and a larger velocity amplitude (Δv, see Table 1) than model M1, chosen so that it produces

TABLE 1

JET MODELS[a]

Model	v_0	Δv	τ_v	n_{ion}
	[km s^{-1}]		[yr]	cm^{-3}
M1	150	0	...	10
M2	150	50	2000	10
M3	150	50	1000	10
M4	200	100	1000	1

[a]All the models have initial jet and neutral cloud densities of 1000 cm^{-3}, jet temperature $T_j = 1000$ K, cloud temperature $T_c = 100$ K, H II region temperature $T_{ion} = 10^4$ K, and jet radius $r_j = 2.5 \times 10^{16}$ cm.

TABLE 2

PEAK Hα FLUXES[a]

Model	$I_{\mathrm{H}\alpha,1}$	$I_{\mathrm{H}\alpha,2}$	$I_{\mathrm{H}\alpha,3}$
	[10^{-3}	erg s^{-1}	cm^{-2} sterad^{-1}]
M1	1.78	...	...
M2	1.48	1.40	...
M3	1.29	1.34	1.12
M4	0.39	1.23	1.04

[a]Peak Hα fluxes corresponding to the working surfaces of the Hα maps shown in Fig. 2.

knots at approximately the same positions as model M3 (by the time that both jets have reached the end of the computational domain, see Figure 2). For this model, we have chosen a combination of higher jet velocity and lower H II region density so as to have a non-radiative bow shock (with an on-axis cooling distance of ~ 10 times the initial jet diameter).

The 3D numerical simulations have been computed on a 5-level, binary adaptive grid with the yguazú-a code. This code has been described in detail by Raga, Navarro-González, & Villagrán-Muniz (2000a), and has been tested with laboratory experiments of jets (Raga et al. 2001) and explosions (Sobral et al. 2000; Velázquez et al. 2001).

The adaptive grid has a maximum resolution of 7.8×10^{15} cm (along the three axes). However, the maximum resolution is only allowed within the region occupied by jet material, so that the leading bow shock as well as the neutral cloud/H II region boundaries are followed with only one half of the maximum resolution (in other words, with a grid of 1.56×10^{16} cm spacing). At this limited resolution, the cooling distances behind the leading bow shock for models M1-M3 (once they have emerged into the H II region) are only resolved by one grid point (the leading bow shock of model M4 being basically non-radiative, see above).

The version of the code that we have used integrates the gasdynamic equations, an advection/rate equation for the density of neutral hydrogen (which includes radiative recombination, and collisional and photo-ionization), and an advection equation for a passive scalar (which is used to label different regions of the flow). Also, the radiative transfer of the ionizing photons (from a source at infinity) is computed, assuming that all the photons are at the Lyman limit (i.e., the hardening of the photons is not included).

The computed photon flux is then used to calculate the hydrogen photoionization rate and heating (included in the neutral hydrogen rate equation and in the energy equation, respectively). A parametrized cooling function (computed as a function of the temperature, density and hydrogen ionization fraction) is also included in the energy equation. A detailed discussion of the ionization/recombination and the heating/cooling rates is given by Cantó et al. (1998) and Masciadri & Raga (2001).

In the initial configuration, hydrogen is fully ionized in the H II region, and neutral in the cloud and in the jet. A seed electron density (assumed to come from singly ionized carbon) is present in the cloud and jet gas.

The results from the four computed models (see Table 1) are described in the following section.

3. MODEL RESULTS

As described in § 2, we have computed four models with the parameters given in Table 1. Fig. 2 shows some of the results obtained for time-integrations $t = 7200$, 6800, 7200, and 4400 yr (for models M1, M2, M3, and M4, respectively). At these times, the leading bow shocks of the jets have reached a distance of $\approx 2 \times 10^{18}$ cm from the injection point.

In model M1 (which is ejected with a constant velocity, see Table 1), a single working surface is formed at the head of the jet. This working surface has a narrow, ionized post-bow shock region, which is followed by a dense, mostly neutral clump. This neutral clump traps an ionization front, as shown by the $n_{H\ II}/n_H = 0.5$ and the $\tau_{\nu_0} = 1$ contours (where $\tau_{\nu_o} = \sigma_{\nu_0} \int_z^D n_{H\ I} dz'$ is the optical depth at the Lyman limit). Such leading working surfaces trapping ionization fronts have been previously modeled by Masciadri & Raga (2001).

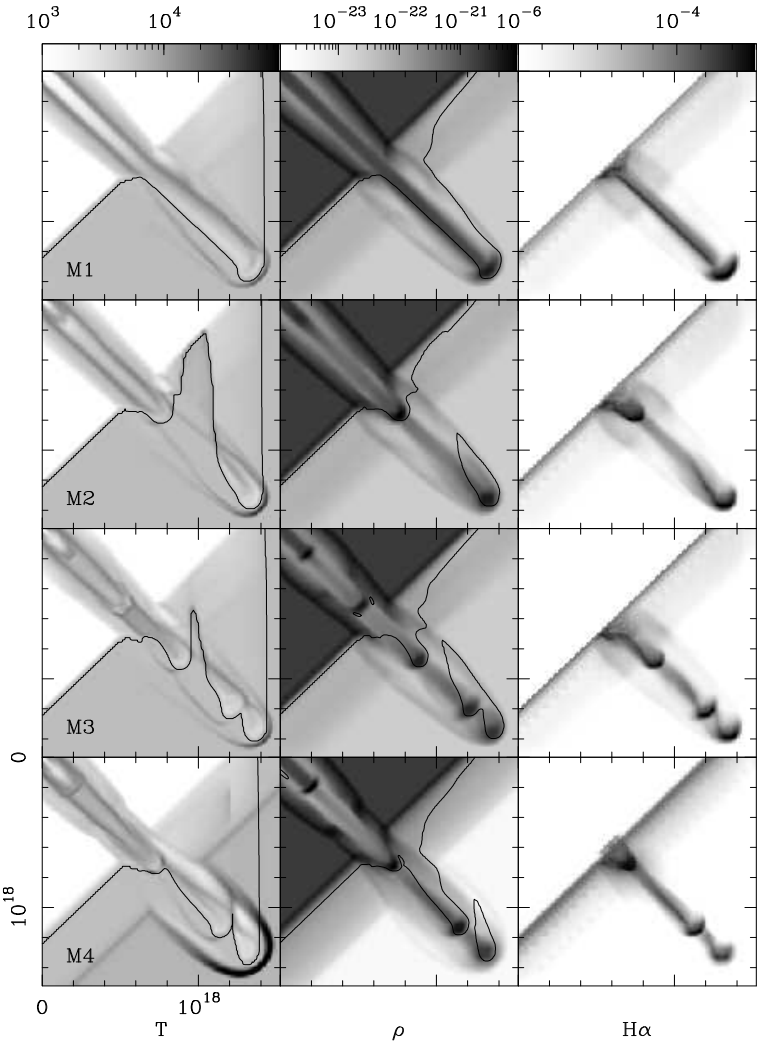

Fig. 2. Temperature (left, plotted with a logarithmic scale depicted in K by the bar at the top), density (center, plotted with a logarithmic scale depicted in g cm^{-3} by the bar) on the $y = 0$ plane, and Hα maps (right, plotted with a logarithmic scale depicted in erg s^{-1} cm^{-2} sterad^{-1} by the bar) obtained from our four models (see Table 1). The Hα maps have been computed assuming that the xz-plane coincides with the plane of the sky. The $\tau_{\nu_0} = 1$ contour is shown on the temperature stratifications (left) and the $n_{H\ II}/n_H = 0.5$ contour is shown on the density stratifications (center). The x (horizontal) and z (vertical) axes are labeled in cm, with the origin of the coordinate system coinciding with the injection point (see Fig. 1). The results shown correspond to time integrations of $t = 7200$, 6800, 7200, and 4400 yr for models M1, M2, M3, and M4, respectively. At these integration times, the jets have reached a total length of $\approx 2 \times 10^{18}$ cm (measured from the injection point to the tip of the leading bow shock).

In model M1, the beam of the jet also traps an ionization front, and has a photoionized region towards the ionizing photon source, and a neutral region away from it (see Fig. 2). Analytical and numerical models of partially photoionized jet beams have been previously discussed by Raga et al. (2000b).

In the other jet models (see Fig. 2), the density in the continuous, inter-working surface jet beam segments is reduced by the "stretching effect" described by Raga & Kofman (1992), so that they become almost fully photoionized. In this way, the working surfaces become isolated, partially neutral "clumps" travelling within a fully photoionized medium.

The four models share in common the following property. In the region within the jet cloud, the jet beam narrows as it propagates away from the injection point. This is due to the fact that the jet is surrounded by a cocoon with a pressure which is higher than the injection pressure (the pressure in the cocoon is also higher than the pressure of the

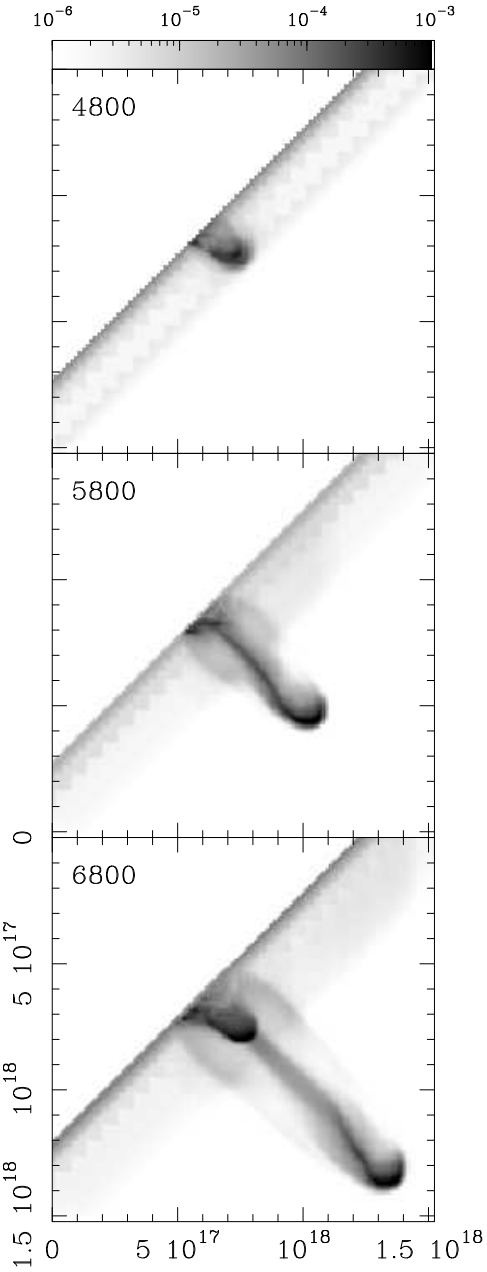

Fig. 3. Time-series of Hα maps obtained from model M2. The plots are labeled with the corresponding integration times (in years). The Hα maps (shown with the logarithmic greyscale depicted in erg s^{-1} cm^{-2} sterad^{-1} by the bar on the top) have been computed assuming that the xz-plane coincides with the plane of the sky. The extinction of the undisturbed cloud material hides the region of the jet within the cloud.

neutral cloud).

As soon as the jet beam emerges into the H II region, it is released from this confining pressure, and expands in a Mach cone. This expansion is seen in all the models that we have computed. By the times that the jets reach a distance of 2×10^{18} cm from the source (i.e., the times shown in Fig. 2), the leading bow shock has a diameter of $\approx 3 \times 10^{17}$ cm (≈ 6 times the initial jet diameter) for models M1, M2, and M3. Model M4 shows a substantially broader bow shock (see Fig. 2), which is a direct result of the fact that for the higher jet velocity and lower H II region density of this model (see Table 1), the bow shock is non-radiative.

In Fig. 2, we also show Hα emission maps. To compute these maps, we have first calculated the Hα emission coefficient, including the recombination cascade and collisional excitations from the $n = 1$ to the $n = 3$ levels. We have then assumed that the xz-plane is parallel to the plane of the sky, and integrated the emission coefficient with respect to the y-coordinate in order to obtain the emission maps. We have also assumed that the lines of sight through the cloud have an optical depth of 50 (at Hα) due to dust extinction, so that the region of the jet within the cloud is basically invisible. We have assumed that the jet material, as well as all the gas with $T > 1000$ K, is dust-free (this includes the H II region gas, and the heated and photoionized cloud gas within the photoevaporated wind).

The Hα map of model M1 shows a strong bow-like emission from the leading working surface. Also, the photoionized edge of the jet beam produces a straight, Hα filament which joins the head of the jet to the surface of the neutral cloud (see Fig. 2). The other three models show two or more working surfaces (all of them with remarkably similar emission structures), and also some emission from the photoionized jet beams (though this emission is fainter than the one shown by model M1). The emission from the jet beam shows a filamentary structure which ends in the wing of the working surface directed towards the ionizing photon source. Interestingly, the wide bow shock of model M4 is not visible in the Hα map, so that the leading working surface of this model actually has a size similar to the ones of the other three models.

An interesting result that can be appreciated in Fig. 2 is that all the working surfaces (regardless of the model or of whether or not it is the leading working surface) show very similar Hα fluxes. This result is quantified in Table 2, where we give the peak Hα intensities of all observed working surfaces (indicating with subscript 1 the leading working surface, with subscript 2 the one closer to the source, and with subscript 3 the third working surface). With the exception of the leading working surface of model

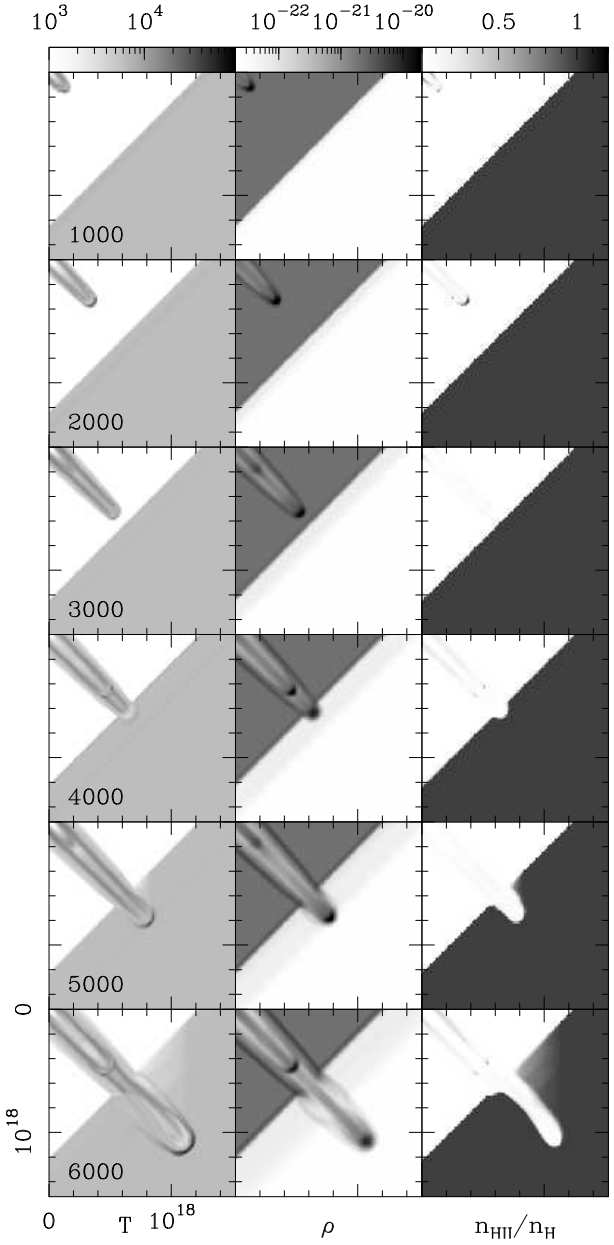

Fig. 4. Temperature (left), density (center) and ionization fraction (right) stratifications on the xz-plane for a time-series obtained from model M2. The greyscales are depicted (in K, g cm^{-3} and unitless, respectively) by the three bars at the top. The successive rows are labeled with the corresponding integration times (in years).

M4 (which has a somewhat lower intensity, see Table 2), all working surfaces have peak intensities $I_{H\alpha} = (1.3 \pm 0.4) \times 10^{-3}$ erg s^{-1} cm^{-2} sterad^{-1}. Interestingly, this result is also obtained for other jet models which we have computed (not shown in the present paper) with the same impinging photoionizing photon flux but with other parameters (e.g., with different velocity variabilities and initial jet densities).

At first glance, this result is quite surprising, since the Hα emission from shocks is strongly dependent on the shock velocity (see e.g., Hartigan, Raymond, & Hartmann 1987). Because of this, models of jets generally predict Hα intensities which are a strong function of the model parameters, and also (in the case of jets from a variable source) are strongly time-dependent (see e.g., Raga et al. 2002). However, in the present models the Hα emission is dominated by the effect of the photoionizations, and not by shock excitation.

One can then construct a simple model to explain the observed Hα intensity. Because the work-

ing surfaces all trap an ionization front, the number of recombinations within a unit area has to be balanced by the impinging flux of ionizing photons. In other words $F_0 = n^2 \alpha_B \delta$, where n is the average density of the working surface, δ is the width of the photoionized layer and α_B is the case B recombination coefficient. The Hα intensity emitted by this layer is then $I_{\rm H\alpha} = n^2 \alpha_{\rm H\alpha} \delta \, h\nu_{\rm H\alpha}/4\pi$, where $\alpha_{\rm H\alpha}$ is the effective Hα recombination coefficient and $h\nu_{\rm H\alpha}$ is the energy of the Hα transition. From the value $F_0 = 1.6 \times 10^{10}$ s^{-1} of our simulations (see the beginning of §2) and the values of α_B and $\alpha_{\rm H\alpha}$ at 10^4 K, we can then estimate the Hα intensity that would be expected for the working surfaces as $I_{\rm H\alpha} = F_0 \, (\alpha_{\rm H\alpha}/\alpha_B)(h\nu_{\rm H\alpha}/4\pi) = 1.75 \times 10^{-3}$ erg s^{-1} cm^{-2} sterad^{-1}. This value is in excellent agreement with the intensities found for the working surfaces of our jet simulations (see Table 2).

As can be seen from Fig. 2, the Hα intensity contrast between the working surfaces and the continuous jet beam segments is only ~ 1 order of magnitude (while the corresponding density contrast is ~ 2 orders of magnitude). This is in clear disagreement with predictions from purely shock-excited variable HH jet models (i.e., without the presence of an external photoionizing photon field), which typically show a factor of $\sim 10^3$ contrast between the Hα intensity of the knots and the continuous beam segments (see, e.g., Raga et al. 2002). On the other hand, the knot/jet beam density contrasts found from purely shock excited jet models are similar to the ones found for the present, photoionized jet models (Raga et al. 2002). These results are due to the fact that while in our present models the dynamical properties of the flow are controlled by the time-dependent ejection, the shock excitation on the other hand produces only a small contribution to the predicted Hα emission.

4. TIME SERIES FROM MODEL M2

In this section, we concentrate on model M2 (see Table 1), and describe the time evolution of the jet. In Figure 3, we show a time series of the Hα maps as the jet emerges from the neutral cloud. At $t =$ 4800 yr, the leading working surface shows up like a "hump" protruding beyond the bright edge of the neutral cloud.

At $t = 5800$ yr, a more jet-like structure is observed (with a length-to-width ratio of ~ 3, see Fig. 3). At this time, a second working surface is just starting to protrude beyond the edge of the dark cloud.

At $t = 6800$ yr, the leading working surface has progressed to a distance of $\approx 10^{18}$ cm beyond the cloud edge. By this time, the second working surface has caught up with the leading working surface, and a third working surface is already starting to emerge from the dark cloud.

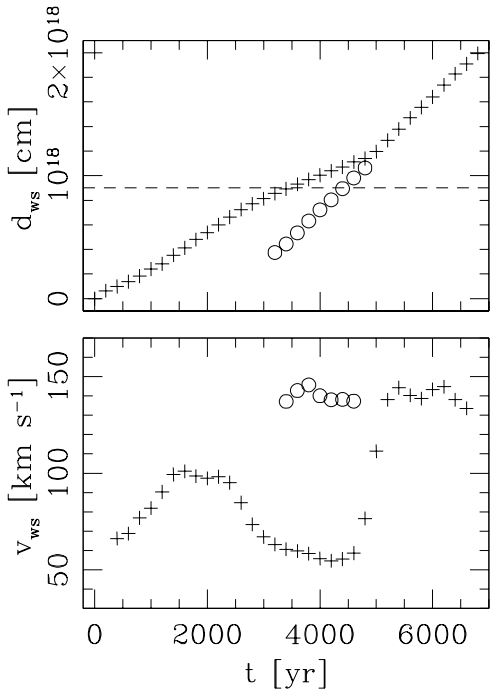

Fig. 5. Distance from the injection point to the leading bow shock (top, crosses) and on-axis bow shock velocity (bottom, crosses) as a function of time, obtained from model M2. The position (top) and the velocity (bottom) of the second working surface (which is formed by the time-variability of the injection velocity) are shown with the open circles. At $t \approx 4800$ yr, the second working surface catches up with the leading working surface. The horizontal, dashed line (top) gives the position of the initial dense cloud/H II region boundary. The values of v_{ws} have been computed by taking centered time-differences of the measured values of d_{ws}, and then applying a 1-2-1 filter (in order to get rid of the noise that is introduced by the differencing procedure).

The three Hα maps of Fig. 3 give an idea of the time-dependent morphologies that are predicted from our jet models. Again, we find that the Hα intensity is very stable, having values of 0.59, 1.6, and 1.5×10^{-3} erg s^{-1} cm^{-2} sterad^{-1} (i.e., close to the "photoionization balance" value, see §3) for the head of the jet at times $t = 4800$, 5800, and 6800 yr, respectively. In the $t = 6800$ yr map, the working surface that is just emerging from the cloud has a peak Hα intensity of 1.4×10^{-3} erg s^{-1} cm^{-2}.

In order to clarify the rather complex dynamics of model M2, in Figure 4 we show a time-series of the temperature, density and hydrogen ionization fraction stratifications on the xz-plane. Initially, as the

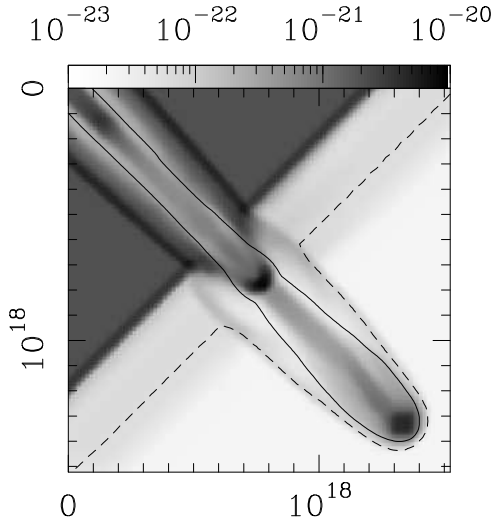

Fig. 6. Density stratification on the xz-plane obtained for a $t = 6800$ yr time-integration from model M2 (shown with the greyscale given in g cm^{-3} by the top bar). The solid contour shows the interface between the jet material and the material that originally belonged to the neutral cloud. The dashed contour shows the interface between the material that originally belonged to the cloud and the H II region material.

jet progresses away from the source, a leading working surface is formed. As a result of the initially rising ejection velocity (see Eq. 1), the temperature and density of the material within the working surface also rise (see the $t = 1000$ and 2000 yr frames of Fig. 4). However, when the material of the first "ejection episode" (i.e., the first period of the sinusoidal ejection velocity variability) is already mostly incorporated into the working surface, the head of the jet starts to slow down as it incorporates an increasing amount of cloud material. This results in a drop of the temperature, density and ionization fraction of the leading working surface (see the $t = 3000$ yr frames of Fig. 4).

In the $t = 5000$ yr frame, we see that the temperature and the density of the head of the jet have again increased. This is a result of the fact that the second working surface (which can be seen travelling away from the source in the $t = 4000$ yr frames of Fig. 4) has caught up with the head of the jet. In the $t = 6000$ yr frames, a third working surface is approaching the edge of the dark cloud.

The dynamics of the first two working surfaces are shown in a more quantitative way in Figure 5. This figure shows the distance d_{ws} from the source to the leading (crosses) and the second (circles) working surfaces (as well as the velocities obtained from time-differencing the d_{ws} values) as a function of integration time t.

At $t = 200$ yr, the leading working surface has a velocity of ≈ 65 km s^{-1}. The velocity of the head of the jet then increases up to a value of ≈ 100 km s^{-1} at $t = 1800$ yr.

It then coasts at approximately the same velocity, as it continues to incorporate fast-moving material ejected from the source. Then, at $t > 2200$ yr, the head of the jet starts to slow down quite dramatically down to a value of ≈ 60 km s^{-1} at $t = 3400$ yr. This slowing down occurs because the high velocity material of the first period of the sinusoidal ejection velocity variability has all been already incorporated into the head of the jet, and the working surface then continues coasting along, incorporating more and more low-momentum, environmental, material.

The slowing-down rate of the head of the jet decreases quite considerably for $t \geq 3400$ yr, since it has now emerged into the low density H II region (see the top plot of Fig. 5). It then coasts along at a velocity of ≈ 60 km s^{-1} until a time $t = 4800$ yr, when it is caught up by the second working surface.

The second working surface (open circles in Fig. 5) develops well defined shocks by a time $t = 2600$ yr. It travels away from the source at an almost constant velocity of ≈ 140 km s^{-1}, until it merges with the head of the jet. Interestingly, beyond the merging point, the leading working surface moves with the same, ≈ 140 km s^{-1} velocity as the second working surface. From the evident momentum conservation argument, this result implies that after the merger, the material in the head of the jet mostly belongs to the second working surface.

Finally, we address the question of the origin of the material that is seen protruding from the neutral cloud at later evolutionary times. To this effect, we have advected a passive scalar, which has a value of 1 for the jet material, -1 for the cloud, and -2 for the material initially within the H II region. In Figure 6, we show the density stratification on the xz-plane for $t = 6800$ yr (model M2), as well as the contours of 0 (separating the jet and cloud material) and -1.5 (separating the cloud and H II region material) for the passive scalar.

In this plot, we see that in the region within the cloud the cocoon has a narrow, inner region made of jet material, and a wide, outer envelope of cloud material (which has been heated and pushed aside by the head of the jet). Outside the cloud, the jet material is surrounded by an envelope of cloud gas which has been dragged out by the jet.

Even though in our simple simulation the properties of this envelope are basically indistinguishable

from the ones of the jet material, in reality this might not be the case. For example, the dragged-out cloud material could have chemical properties that might lead to an observable molecular emission, or could contain enough surviving dust so as to produce an observable extinction.

5. CONCLUSIONS

We have calculated models of an HH jet emerging from a neutral cloud into an H II region. Because the number of possible free parameters in this problem is in principle huge, we have made a very limited exploration of the possible configurations. Because of this, our study is meant only as an illustration of the possible observational properties of this kind of flow.

We have considered a plane neutral cloud/H II region interface, which is illuminated obliquely by the photoionizing source. The HH jet axis is assumed to be perpendicular to the interface. We have also assumed that the jet has an initial density which is equal to the cloud density, and then emerges into the H II regions as a highly overdense jet. We have then run four models, one with a time-independent ejection velocity, and three with sinusoidal variabilities of different mean velocities, periods and amplitudes.

The Hα intensity maps predicted from our four models (see Table 1) all show one or more arc-like structures (produced by the successive working surfaces). The morphologies of all working surfaces are very similar to each other (regardless of the model or of whether or not they are the leading working surface). Also, the Hα intensities of the working surfaces are most similar (see Table 2).

This is due to the fact that the working surfaces basically behave as neutral clumps which are bathed by the impinging ionizing photon field. Therefore, their emission properties are to a large extent determined by the impinging photon field rather than by the dynamical properties of the working surfaces themselves. We find that if we consider the balance between the ionizing photon flux and the radiative recombinations within the photoionized layer of the working surface, we obtain a prediction for the emitted Hα intensity which is in excellent agreement with the predictions obtained from our numerical simulations (see § 3).

We then conclude that if we have jets with working surfaces that trap an ionization front, the radiative properties of the working surfaces should reflect the intensity of the impinging ionizing photon field, and should not depend strongly on the parameters of the jet flow. In this way, observations of HH jets emerging into an H II region could be used to probe the spatial dependence of the ionizing photon field.

A similar technique has of course already been used in order to study the Helix nebula, which has a large number of embedded (but quasi-stationary) neutral clumps (see López-Martín et al. 2001, and references therein).

The work of ACR was supported by CONACyT grant 36572-E and DGAPA (UNAM) grant IN 112602. BR acknowledges support from NASA grant NAGW-3192 (LTSA).

REFERENCES

Bally, J., Reipurth, B., Walawender, J., & Armond, T. 2002, AJ, 124, 2152
Cantó, J., Raga, A. C., Steffen, W., & Shapiro, P. 1998, ApJ, 502, 695
Hartigan, P., Raymond, J. C., & Hartmann, L. W. 1987, ApJ, 316, 323
López-Martín, L., Raga, A. C., Mellema, G., Henney, W. J., & Cantó, J. 2001, ApJ, 548, 288
Masciadri, E., & Raga, A. C. 2001, A&A, 376, 1073
Raga, A. C., & Kofman, L. 1992, ApJ, 386, 222
Raga, A. C., López-Martín, L., Binette, L., López, J. A., Cantó, J., Arthur, S. J., Mellema, G., & Steffen, W. 2000b, MNRAS, 314, 681
Raga, A. C., Navarro-González, R., & Villagrán-Muniz, M. 2000a, RMxAA, 36, 67
Raga, A. C., Sobral, H., Villagrán-Muniz, M., Navarro-González, R., & Masciadri, E. 2001, MNRAS, 324, 206
Raga, A. C., Velázquez, P. F., Cantó, J., & Masciadri, E. 2002, A&A, 395, 647
Reipurth, B., & Bally, J. 2001, ARA&A, 39, 403
Reipurth, B., Armond, T., Raga, A. C., & Bally, J. 2003, ApJ, 593, L47
Reipurth, B., Yu, K.C., Moriarty-Schieven, G., Bally, J., Aspin, C., & Heathcote, S. 2004, AJ, in press
Sobral, H., Villagrán-Muniz, M., Navarro-González, R., & Raga, A. C. 2000, App.Phys.Lett., 77, 3158
Velázquez, P. F., Sobral, H., Raga, A. C., Villagrán-Muniz, M., & Navarro-González, R. 2001, RevMexAA, 37, 87

Alejandro C. Raga: Instituto de Ciencias Nucleares, UNAM, Apartado Postal 70-543, 04510 México, D. F., México. (raga@nuclecu.unam.mx)
Bo Reipurth: Institute for Astronomy, University of Hawaii, 2680 Woodlawn Drive, Honolulu, HI 96822, USA (reipurth@ifa.hawaii.edu).